Confined hot-pressurized water in Brønsted-acidic beta zeolite speeds up the *O*-demethylation of guaiacol

Massimo Bocus [1], Elias Van Den Broeck[1,4], Xian Wu[2,4], Mathias Bal [3,4], Jeroen Bomon [3], Louis Vanduyfhuys[1], Bert F. Sels [2], Bert U. W. Maes [3] & Veronique Van Speybroeck [1]

Biorefinery technologies that convert lignin into platform chemicals are essential to reduce our future dependence on fossil resources. In these technologies, a key process is the acid-catalysed *O*-demethylation of guaiacol derivatives in hot-pressurized water using Brønsted mineral acids or microporous zeolites. The fundamental understanding of how hydronium ions behave in a confined environment versus bulk is still limited. Here we investigate the *O*-demethylation of guaiacol in hot-pressurized water with HCl or H-BEA zeolite catalysts to elucidate the impact of zeolite microporosity on reaction mechanisms and rates. Operando molecular simulations combined with experimental kinetic studies reveal that, regardless of the catalyst type, *O*-demethylation follows a concerted
O-activated S_N2 mechanism. The reaction rate is higher in the zeolite due to more active, under-coordinated hydronium ions. Additionally, the molecular organization of solvent and reactants around the confined active site plays a crucial role in modulating the association of the reacting species and the reaction kinetics.

It is now undeniable that reducing CO_2 emissions is crucial to effectively combat climate change. A fundamental shift is needed to transition from a take–make–consume–dispose model to a take–make–consume–recycle approach. In practice, this requires adopting a circular chemical economy, which involves replacing fossil carbon sources with renewable ones[1,2]. Abundantly available lignocellulosic biomass has the potential to become part of the feedstock mix for sustainable carbon sources[1]. This will only be possible if biorefineries can efficiently upgrade the entire biomass—both the lignin and carbohydrate fractions—into viable and valuable product streams[3–5]. To achieve this ambitious goal, various lignin-first conversion technologies are currently under development[5–7].

Lignin is the largest renewable source of aromatics and consists of *p*-coumaryl, coniferyl and sinapyl alcohol units connected through C–O and C–C crosslinkages[7–11]. With the most recent advances in lignin-first biorefineries, wood lignin can be efficiently depolymerized into lignin oils rich in a handful of guaiacol and syringol derivatives, hereby valorizing both the carbohydrate and lignin part of wood[5–7]. Furthermore, these derivatives can be chemically tailored to improve their economic potential, producing, among others, drop-in catechol and phenol with a large petrochemical market[12]. The lignin oil can also be modified and applied in the synthesis of, for example, antioxidants and anticorrosion and chelating agents, or used as a precursor in the production of fine chemicals and new (biodegradable) polymeric materials[5,11–17].

To access drop-in catechol from lignocellulose biomass, the *O*-demethylation of guaiacol is a crucial reaction for which a variety of synthetic procedures have been reported[18]. They typically entail harsh reaction conditions and superstoichiometric amounts of hazardous,

[1]Center for Molecular Modeling, Ghent University, Zwijnaarde, Belgium. [2]Center for Sustainable Catalysis and Engineering, KU Leuven, Leuven, Belgium. [3]Organic Synthesis Division, Department of Chemistry, University of Antwerp, Antwerp, Belgium. [4]These authors contributed equally: Elias Van Den Broeck, Xian Wu, Mathias Bal. e-mail: bert.sels@kuleuven.be; bert.maes@uantwerpen.be; veronique.vanspeybroeck@ugent.be

non-sustainable reagents in undesirable solvents, and also produce problematic by-products[18–20]. In principle, sustainable and scalable *O*-demethylation should be selective with a high yield and preferably performed in a green solvent such as water[3,20,21]. To this end, recent studies have shown the potential of Brønsted acid catalysis for the *O*-demethylation reaction in subcritical hot-pressurized water (HPW)[20,22–25]. At high temperatures, water behaves similarly to an organic solvent due to its reduced dielectric constant, offering great opportunities in the context of green organic chemistry. For instance, we recently showed that 20 mol% HCl in HPW can convert guaiacol into catechol with 97% yield[20] (Fig. 1a). The main drawback in the process lies in the high corrosivity of aqueous mineral acids, requiring a Hastelloy reactor material that increases the overall capital expenditure.

Solid acids offer a non-corrosive alternative to mineral acids and provide the traditional technological benefits of heterogeneous over homogeneous catalysis. Acidic zeolites, in particular, are crystalline microporous inorganic materials known for their exceptional catalytic activity and selectivity, playing a crucial role in modern fossil feedstock refining. Although they typically require modifications to maintain stability in water, these zeolites could also become central to the emerging biorefinery industry[3,26,27]. Recently, acidic beta zeolite (H-BEA, *BEA topology) was identified as an effective catalyst for the *O*-demethylation of 4-propylguaiacol, a major product in lignin oil derived from the lignin-first biorefinery of softwood[27]. This reaction, carried out in HPW, produces 90% 4-propylcatechol, which can then be converted to catechol through subsequent retro Friedel–Crafts cleavage of the propyl group.

The presence of water influences substantially the catalytic properties of Brønsted acid sites in zeolites[28–32]. For example, Lercher and colleagues have demonstrated that hydronium ions (H_3O^+) trapped within the microscopic voids of zeolites exhibit higher activity for the monomolecular dehydration of cyclohexanol compared to bulk solution[33]. They suggest that the intense ionic environment within zeolite micropores—resulting from the net charge separation between negatively charged aluminium defects and water clusters containing hydronium ions—affects the chemical potential of the reacting species, thereby greatly enhancing reactions between charged partners[34–36]. Despite these experimental findings, the fundamental differences between hydronium ions in bulk water and those in confined environments remain unexplored. Additionally, it is uncertain how these results might apply to other reaction systems, such as bimolecular reactions like hydrolysis, which may not involve charged intermediates in the rate-determining step, or systems where water itself acts as a reagent. Understanding these aspects is essential for elucidating and optimizing critical reactions that take place in confined aqueous environments.

In this study, we present a combined computational and experimental investigation of the acid-catalysed *O*-demethylation of guaiacol to catechol, a model bimolecular reaction in water, using both homogeneous (HCl) and heterogeneous (H-BEA zeolite) catalysts (Fig. 1b). Here, water acts as both the solvent and reactant. We employ enhanced-sampling ab initio molecular dynamics (AIMD) simulations under operando conditions, in conjunction with experimental kinetic measurements, to uncover the reaction mechanism and determine the rate constants of the reactive steps. This approach provides detailed molecular-level insights into the differences in hydronium ion activity between homogeneous (non-confined) and heterogeneous (confined) catalytic systems in the bimolecular *O*-demethylation reaction.

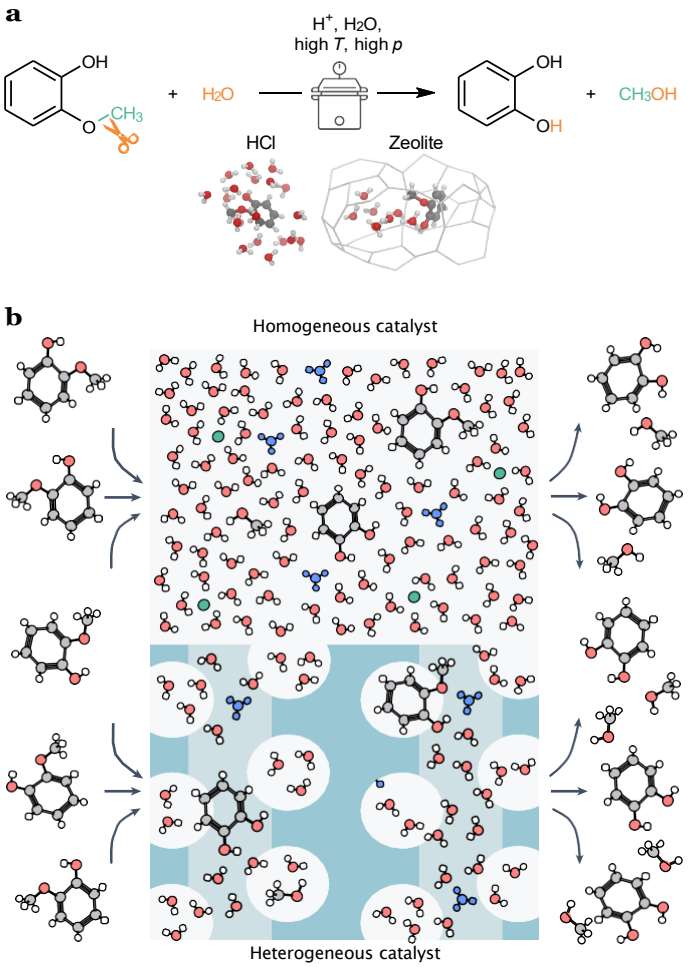

Fig. 1 | Homogeneously versus heterogeneously catalysed O-demethylation of guaiacol in HPW. a, General reaction scheme for the *O*-demethylation of guaiacol. *T*, temperature; *p*, pressure. **b**, Schematic, hypothetical depiction of the investigated systems: the homogeneous conversion using aqueous HCl and the heterogeneous one using H-BEA (O is red, C is grey, H is white and Cl is green; hydronium ions are emphasized with a blue colour).

Results

Mechanism and reactivity of the guaiacol *O*-demethylation

The *O*-demethylation reaction of guaiacol to catechol was experimentally studied in HPW using both a homogeneous (HCl, 508–543 K) and a heterogeneous (H-BEA zeolite, 479–497 K) Brønsted acid catalyst. Remarkably, hydronium ions in H-BEA zeolite are more effective at catalysing the reaction compared to those in bulk water (Fig. 2). The Arrhenius activation energy decreases from 147 ± 8 kJ mol^{-1} in the homogeneous system to 111 ± 6 kJ mol^{-1} in the heterogeneous system. Such acceleration is therefore not unique for monomolecular alcohol dehydration[33], but occurs in bimolecular reactions as well, where water acts as a reactant rather than a product.

To investigate the detailed atomistic origins of this intriguing feature, we conducted an operando theoretical study that accounts for the complexity of the reaction conditions. Our first step was to examine the reaction mechanism, as understanding the preferred reaction pathway is crucial for assessing how it is influenced by different reaction environments. Building on previous mechanistic proposals, we explored three potential pathways for the *O*-demethylation reaction[20,22–25] (Fig. 3a).

The first pathway, which our simulations suggest is the most favourable, involves an O-activated S_N2 mechanism. There, the methoxy group is activated through protonation and then attacked by a nucleophilic water molecule. While the common literature hypothesis posits that the reaction proceeds through a (meta)stable oxonium ion intermediate, our findings indicate that this intermediate is unstable and only transiently formed en route to the S_N2 transition state (vide infra). Consequently, we will refer to this pathway as the concerted O-activated S_N2 (COA-S_N2) mechanism.

The second and third proposed mechanisms both involve the preliminary activation of the arene ring through *para* protonation, leading to the formation of an activated arenium ion intermediate (**II**). In the second mechanism, a nucleophilic water molecule directly attacks the methyl group, producing the cyclohexadienone intermediate **IV**. In the third mechanism, water attacks the *ipso* aromatic carbon, forming a hemiacetal intermediate (**III**), which then eliminates methanol to yield the cyclohexadienone intermediate **IV**. In both cases, a final isomerization converts the cyclohexadienone into the final product (**VI**) through a protonation–deprotonation mechanism involving intermediate **V**.

All reaction steps were thoroughly examined using enhanced-sampling AIMD simulations to capture temperature effects and the high mobility of the reacting species. Figure 3b provides a visual representation of the molecular models used to simulate the two catalytic systems. Kinetic and thermodynamic data were obtained from the simulations using classical transition state theory, as detailed in Methods. The free energy profiles for the two catalytic systems are presented in Fig. 3c.

It is immediately clear that the preferred mechanism is the COA-S_N2, which has a calculated free energy barrier of 112 kJ mol^{-1} in the homogeneous system and 97 kJ mol^{-1} in the heterogeneous system. This indicates a higher reaction rate in the heterogeneous system, which aligns qualitatively with the experimental kinetic results (Fig. 2). We will explore the molecular origins of this observation in detail in the final paragraph of this section, after validating our mechanistic hypothesis.

While the COA-S_N2 mechanism is the most favourable, the protonation of the arene ring (**I** → **II**) has the lowest activation energy but is also highly endothermic. The equilibrium between the neutral and protonated arene will strongly favour the first, meaning that most protons in the system will be in the form of reactive hydronium ions. The low stability of **II** results in higher barriers for the subsequent steps compared to the COA-S_N2 pathway. The C-activated S_N2 reaction (**II** → **IV**) has a barrier of 139 kJ mol^{-1} relative to guaiacol (**I**), compared to 112 kJ mol^{-1} for **I** → **VI** in the homogeneous system and 159 kJ mol^{-1} versus 97 kJ mol^{-1} in the heterogeneous one.

In both systems, the formation of the hemiacetal (**II** → **III**) is the least favourable pathway. Given that the barriers for the C-activated S_N2 and hemiacetal formation are high enough to make these mechanisms unlikely, we did not further investigate the steps **III** → **IV** and **IV** → **VI** in the heterogeneous system. Based on results from the homogeneous system, these steps are both very favourable and do not hinder the formation of catechol. A detailed description of all the reactive steps, along with the computational details and results from the enhanced-sampling simulations, is provided in Supplementary Note 1.

As it is the most favourable mechanism, we will now examine the COA-S_N2 reaction (**I** → **VI**) in greater detail. To achieve this, we monitored the reaction using key collective variables (CVs) that depend on the atomic coordinates and help identify the various stable and metastable intermediates and transition states along the reaction pathway. Throughout this paper, these CVs will be employed to gain chemical insights and to identify reaction intermediates.

The original free energy surface (FES) was obtained in terms of two CVs (Fig. 4a). The first CV (**CV$_1$**) tracks the progress of the S_N2 reaction using a difference of two coordination numbers (CNs; Methods): the CN between the methoxy carbon (C_m) and all water oxygen atoms (O_w), and the CN between the methoxy oxygen (O_m) and C_m. **CV$_1$** ranges from approximately −1 to +1, where in the reactant state, CN(O_m;C_m) is around +1 and CN(C_m;O_w) is close to 0, and vice versa in the product state. The second CV (**CV$_2$**) is defined as a single CN between O_m and all water hydrogen atoms (H_w), including the hydrogen of the hydroxyl group (H_h), which can exchange with water under reaction conditions. Therefore, **CV$_2$** indicates the extent of association between O_m and the system's protons. The two CVs effectively track the activation of the methoxy group by protonation and the subsequent nucleophilic attack by a nearby water molecule.

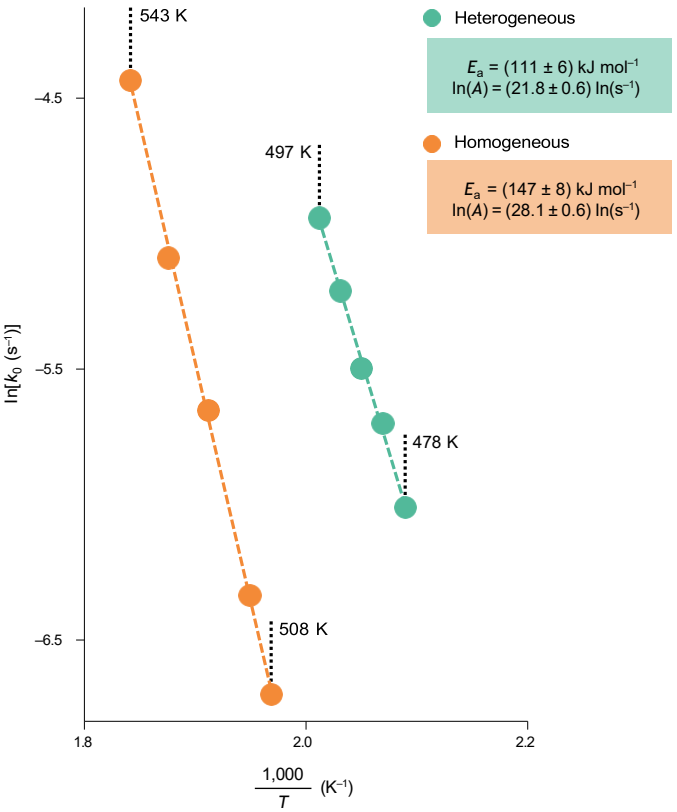

Fig. 2 | O-demethylation of guaiacol in HPW with H-BEA or with homogeneous HCl. The reaction proceeds faster with H-BEA than with HCl, as clearly visible in the experimental Arrhenius plots for the two systems with equimolar hydronium ions. The observed activation energy (E_a) is lower for the heterogeneous system (111 ± 6 kJ mol^{-1}) than for the homogeneous system (147 ± 8 kJ mol^{-1}); k_0 is the kinetic constant at zero-order regime (its calculation is in Supplementary Note 2) and A the pre-exponential factor. The raw data are reported in Supplementary Tables 16 and 23 for the homogeneous and heterogeneous systems, respectively.

Figure 4b,c display the FESs in terms of the two CVs obtained from umbrella sampling (US) in the homogeneous and heterogeneous systems, respectively. The most notable feature of the two FESs is the concerted nature of the reaction. Unlike in previously proposed mechanisms, we do not observe the formation of a stable or metastable oxonium ion intermediate, which would appear as a shallow minimum at **CV$_1$** ≈ −0.8 and **CV$_2$** ≈ 0.8 in Fig. 4b,c, if it were present. Instead, an ionic contact pair forms between the hydronium ion and the guaiacol molecule. At the onset of the S_N2 reaction (**CV$_2$** ≈ 0.8), the proton is almost completely transferred to the guaiacol molecule, while a water molecule remains in close proximity, resulting in a shared proton between the two molecules. Figure 4d,e illustrates how this ionic contact pair appears during one of the AIMD US simulations. Given the unusual nature of this COA-S_N2 mechanism, we conducted additional experiments to further validate the theoretical results.

Evidence for the unusual COA-S_N2 mechanism

To support the COA-S_N2 mechanism predicted by theory, we conducted additional experiments to determine if the experimental observations align with the theoretical predictions.

First, we examined the reaction in the homogeneous system using (other than the *O*-methyl) *O*-alkylcatechol derivatives (ethyl **Ib** and cyclohexyl **Ic**; Fig. 5a). Despite these derivatives making a classical S_N2 reaction more challenging, catechol formation actually occurred more rapidly with more substituted alkyl carbons (that is, methyl **I** < primary **Ib** < secondary **Ic**). This observation aligns with the COA-S_N2 mechanism: a more substituted alkyl carbon enhances the electron density of

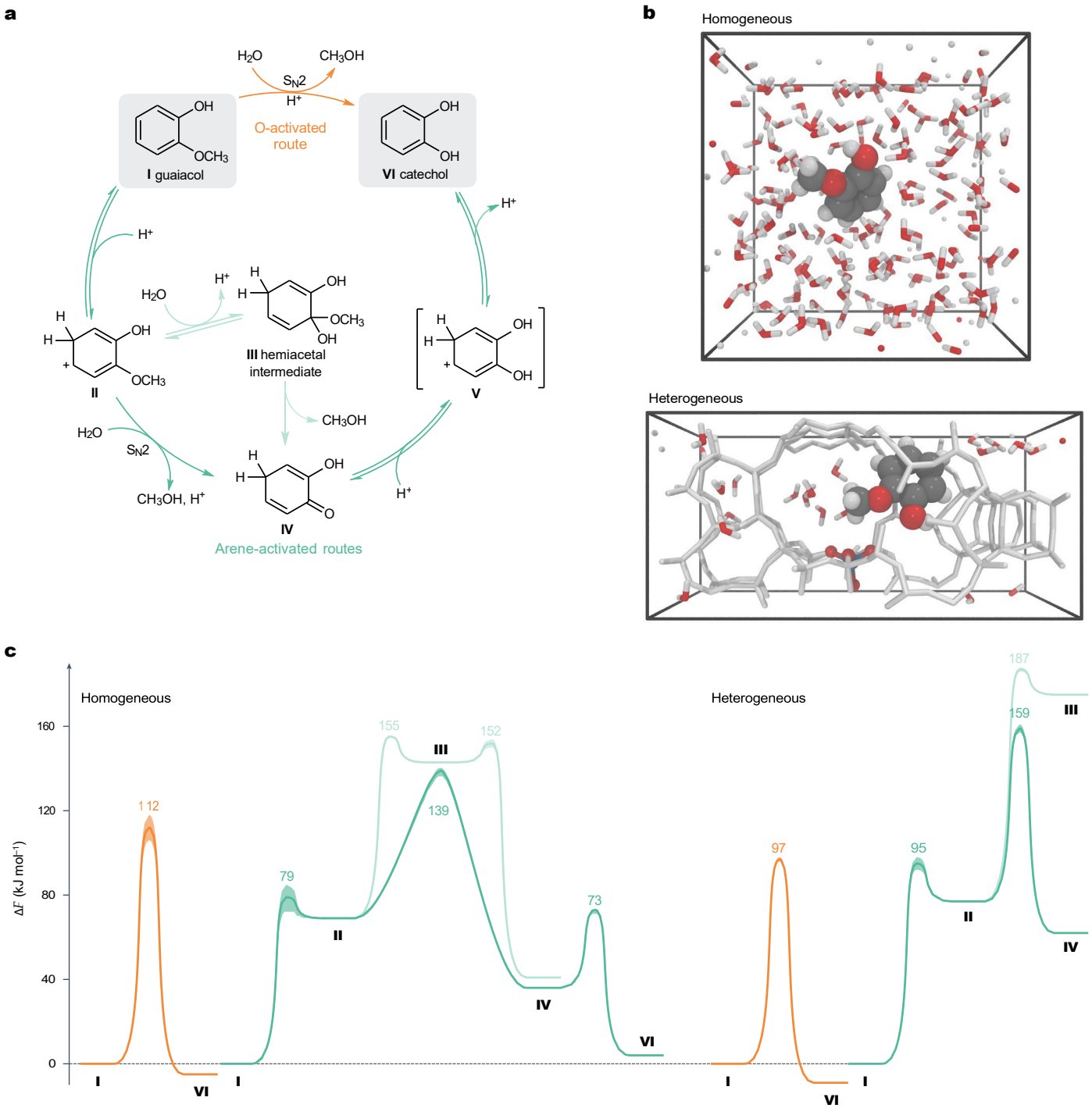

Fig. 3 | O-demethylation of guaiacol in HPW through a COA-S_N2 mechanism. **a**, The three proposed reaction pathways for the *O*-demethylation of guaiacol. **b**, Unit cells of the homogeneous and heterogeneous catalyst models used for the computational investigation (O is red, C is grey, Al is blue and H is white; the guaiacol is in van der Waals representation, while the zeolite framework, aside from the Al tetrahedron, is depicted with white sticks for the sake of clarity). **c**, Free energy (ΔF) profiles for the various *O*-demethylation pathways in the homogeneous and heterogeneous systems. The free energy values are obtained from enhanced-sampling AIMD simulations (BLYP-D3/TZVP) within classical transition state theory (Methods). Note that the errors on the free energy barriers (light-shaded areas) are specific for each step and do not account for the uncertainty on previous steps. Moreover, the alignment of states between different reactions (for example, **II** as product of **I** → **II** and reactant of **II** → **IV**) is done in the approximation that the same phase space is explored. This is reflected in some artefacts such as the misalignment of states **IV** and **VI** when coming from different reactive paths, which however do not impact our conclusions, which are always based on forward reaction barriers.

the oxygen through inductive effects, which facilitates the formation of the ionic contact pair necessary for the S_N2 reaction. By contrast, *O*-phenylcatechol (**Id**; Fig. 5a)—which cannot undergo S_N2—yielded no detectable product, supporting the theoretical predictions that the hemiacetal mechanism, the only alternative for **Id**, is not valid under these conditions (Fig. 3c).

Second, when 20 mol% DCl in D_2O was used with guaiacol (**I**), complete deuteration of the arene ring was observed, as indicated by

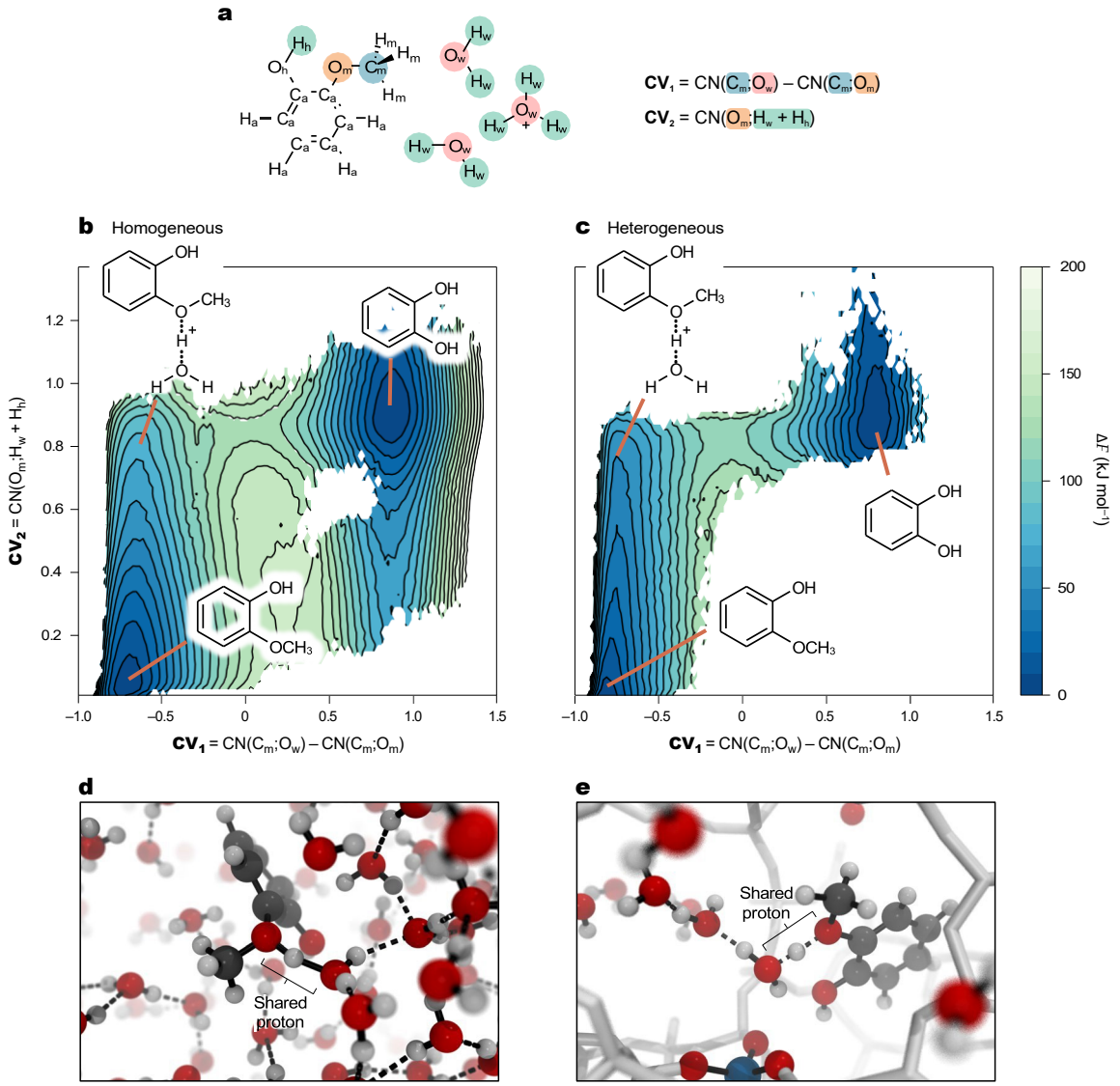

Fig. 4 | The O-activated S_N2 mechanism proceeds without an oxonium intermediate. a, Summary of the two CVs used to describe the reaction. The conventional nomenclature of the main atoms in the system used throughout the paper is also shown. C_a, aromatic carbon; H_a, aromatic hydrogen; O_h, hydroxyl oxygen; H_m, methoxy hydrogen. **b**, Two-dimensional FES for the **I** → **VI** reaction (as defined in Fig. 3) in the homogeneous system, as obtained from US simulations. **c**, Same as in **b**, but for the heterogeneous system. **d**,**e**, Snapshots extracted from the US simulations of the homogeneous (**d**) and heterogeneous (**e**) systems at $\mathbf{CV_1} \approx -0.8$ and $\mathbf{CV_2} \approx 0.8$, highlighting the formation of the ionic contact pair (C is grey, O is red, H is white and Al is blue; all zeolite atoms besides the AlO_4 tetrahedron are shown as white sticks for the sake of clarity).

the disappearance of all aromatic ^{1}H NMR signals for **I**. This deuteration occurred at a lower temperature (185 °C) compared to the *O*-demethylation reaction (225–275 °C), consistent with the low barrier for the **I** → **II** reaction (Fig. 3c).

Third, we investigated the solvent kinetic isotope effect (SKIE) by conducting the reaction in both the homogeneous and heterogeneous systems in H_2O and D_2O. Since theory predicts a complete proton transfer to guaiacol before crossing the COA-S_N2 transition state (Fig. 4b,c), a SKIE of less than one is expected. This was confirmed experimentally, with a strongly inverse SKIE observed, namely, 0.6 for the homogeneous and 0.7 for the heterogeneous system (Fig. 5b,c). To explain this result, it is helpful to consider the observed (obs) SKIE as the product of both primary (prim) and secondary (sec) SKIE contributions:

$$\left(\frac{k_H}{k_D}\right)_{obs} = \left(\frac{k_H}{k_D}\right)_{prim} \left(\frac{k_H}{k_D}\right)_{sec} \quad (1)$$

where k_H and k_D are the reaction rate constants in H_2O and D_2O, respectively. On the one hand, the primary SKIE[37], induced by H atoms directly involved in the rate-determining transition state, will be close to unity according to the simulations, as the COA-S_N2 transition state is crossed once the proton transfer reaction is complete (this is occurring at $\mathbf{CV_2} \approx 0.8$; Fig. 4). The secondary SKIE, on the other hand, involves the non-reacting hydrogen atoms of neutral water. We therefore monitored the protonation state of the closest water molecule to C_m (that is, the one undergoing the nucleophilic attack) during the reaction. For this, we followed the CN between the closest O_w to C_m, which is noted as O_w^N (nucleophilic water oxygen), and all the exchangeable hydrogens in the system, which can take values from ~1 to ~2.5 (Fig. 5f). Figure 5d,e shows the corresponding FESs in terms of $\mathbf{CV_1}$ (as in Fig. 4b,c, this CV is able to monitor the progress of the S_N2 reaction) and $CN(H_w;O_w^N)$ for the homogeneous and heterogeneous systems, respectively. In both cases a neutral water molecule with two H atoms is the only nucleophilic

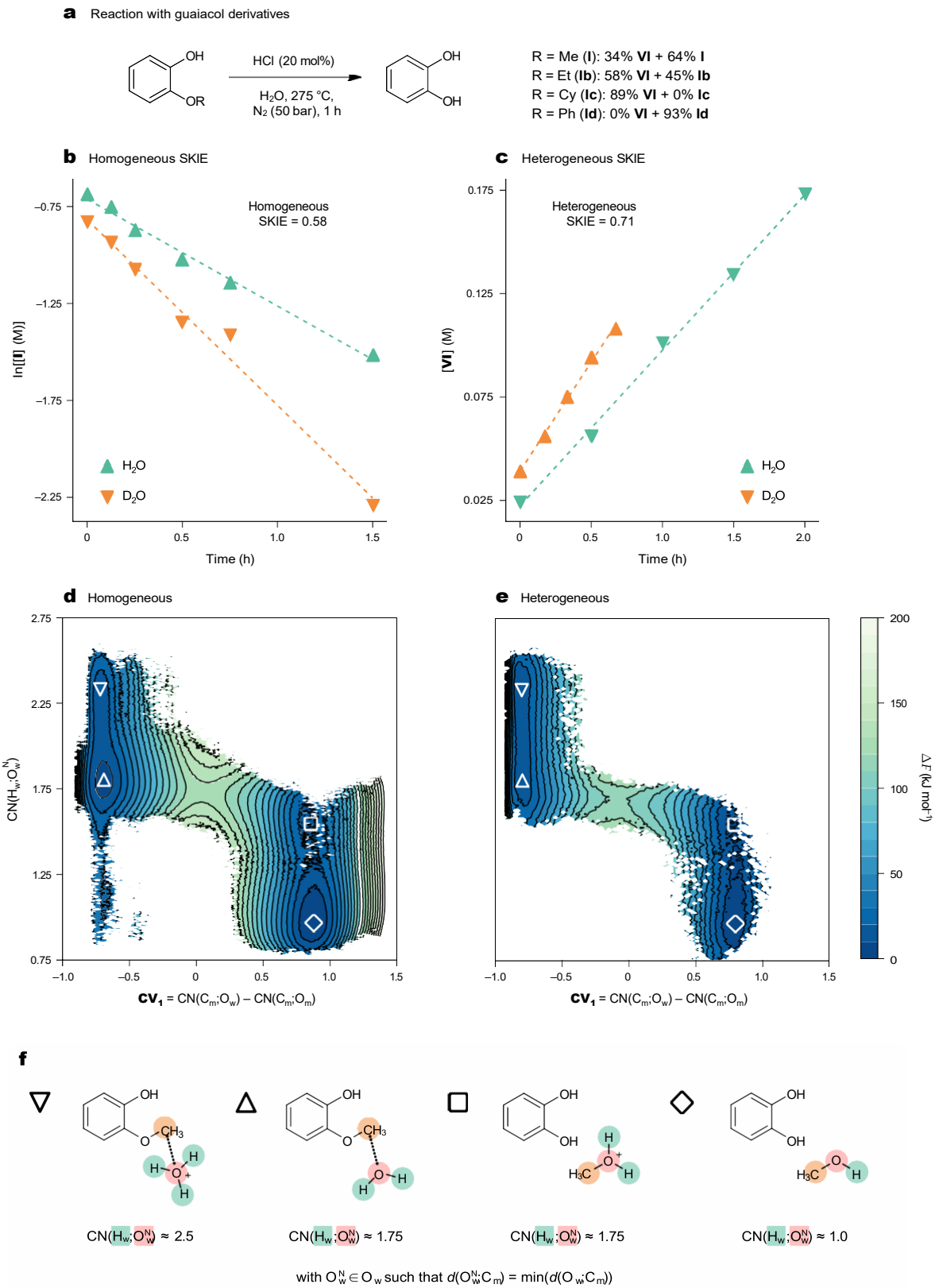

Fig. 5 | Experimental evidence supports the COA-S_N2 mechanism. a, Summary of the reactions conducted in the homogeneous experimental set-up with guaiacol derivatives. **b**, Logarithm of the concentration of guaiacol (**I**; see Fig. 3 for the numbering of the species) versus time in the homogeneous experimental set-up when using H_2O and D_2O (523 K), used to determine the SKIE. The raw data are reported in Supplementary Tables 18 and 19. **c**, Concentration of catechol (**VI**) versus time in the heterogeneous experimental set-up when using H_2O and D_2O (497 K), used to determine the SKIE. The raw data are reported in Supplementary Tables 20 and 24. **d**,**e**, Two-dimensional FESs for the homogeneous (**d**) and heterogeneous (**e**) systems obtained by transforming the FESs in Fig. 4b,c to follow the protonation state of the water molecule closest to the methyl carbon ($CN(H_w; O_w^N)$, d_0 = 1.3 Å; for the definition of d_ϑ see equation 3 in Supplementary Methods) during the COA-S_N2 reaction. **f**, Summary of the intermediates identified by different CV values in **d** and **e**.

species at the transition state ($CN(H_w;O_w^N) \approx 1.75$), and the methanol produced deprotonates only after complete C–O bond breaking. This indicates that two non-reacting hydrogens are strongly contributing to the SKIE at the transition state. Previous reports in the literature have highlighted that such a secondary kinetic isotope effect for non-reacting hydrogen atoms is strongly inverse, for example, with reported values of 0.6, compatible with ours[38].

Rationalizing the higher activity of confined hydronium ions

Building on the experimental support for the COA-S_N2 mechanistic proposal, we examined the atomistic reasons behind the higher activity of H_3O^+ in the H-BEA catalyst compared to homogeneous aqueous HCl. Although theory predicts a lower activation free energy in H-BEA (Fig. 3c), comparing the catalytic systems directly is complicated due to the varying amounts of water molecules in their unit cells (Fig. 3b). This variation hampers the separation of enthalpic and entropic contributions to the computed free energy barrier. To address this, we sought more general descriptors to uncover the reasons for the enhanced activity of confined hydronium ions. We established three additional hypothetical systems for this purpose. The first two systems were designed to vary the amount of water adsorbed in H-BEA. Due to the approximate nature of the methodology used to estimate the original loading of 22 water molecules per unit cell (Supplementary Methods), we recalculated the FESs for the **I** → **VI** reaction with ±5 water molecules (that is, 17 and 27 molecules). The third system investigated the effect of confinement by considering the more spacious large pores of H-FAU zeolite, filled with 22 water molecules in the unit cell. A summary of the computed **I** → **VI** rate constants and phenomenological free energy barriers (Methods) is presented in Table 1.

The results we obtained were quite unexpected. First, regarding the water loading in H-BEA, we observed that increasing the amount of water from 22 to 27 molecules per unit cell led to a moderate reduction in the reaction barrier, from 97 to 90 kJ mol^{-1}. Conversely, reducing the water content from 22 to 17 molecules per unit cell increased the barrier to 110 kJ mol^{-1}, which is quite close to the 112 kJ mol^{-1} observed for the homogeneous case. Hence, increasing the amount of water molecules decreases the free energy barrier. Changing the zeolite framework also had a comparable effect to decreasing the water loading; the computed barrier for H-FAU with 22 water molecules was 116 kJ mol^{-1}, compared to 97 kJ mol^{-1} for H-BEA with the same water loading.

To shed light on this behaviour, we first investigated the interaction between the reacting guaiacol and the hydronium ion. To this end, we focused on the FES region related to the protonation reaction. This means considering $\mathbf{CV_1}$, which monitors the progress of the S_N2 reaction, from –1.0 to –0.25, as shown in Fig. 4b,c (also shown in Fig. 6 for the three catalytic systems) and converting it into a new CV that encodes the protonation state of the closest O_w to O_m (proton-donor water oxygen, O_w^p) as function of the guaiacol protonation progress. This CV is chosen as the CN between O_w^p and all the exchangeable hydrogens in the system. The converted FESs are shown in Fig. 6, together with a three-dimensional representation thereof. Note that $\mathbf{CV_2}$ is kept as the CN between O_m and H_w, similar to in Fig. 4. In the homogeneous system, water is the only species interacting with O_m in the proximity of the reactant region (the down-pointing triangle in Fig. 6a). Only once the protonation reaction is well underway ($\mathbf{CV_2} \approx 0.3$) is the hydronium ion forced into proximity with the guaiacol molecule (the up-pointing triangle in Fig. 6a) and, at the onset of the S_N2 reaction ($\mathbf{CV_2} \approx 0.8$), the protonation state reaches an intermediate value between H_2O and H_3O^+ (the square in Fig. 6a) that corresponds to the ionic contact pair highlighted in Fig. 4d,e. A somehow similar situation can also be seen for H-BEA (22 H_2O) and H-FAU (22 H_2O), reported in Fig. 6b,c, respectively. The main difference is the facility of the association between the guaiacol molecule and the hydronium ion. In H-BEA, interaction with H_3O^+ is already prominent in proximity to the reactant minimum (the down-pointing triangle in Fig. 6b) and becomes predominant as soon as the system begins to climb towards the transition state ($\mathbf{CV_2} \approx 0.3$). H-FAU is somehow in between, where the interaction of guaiacol with H_3O^+ is certainly stronger than in the homogeneous case, but at $\mathbf{CV_2} \approx 0.3$, a substantial interaction still exists with neutral water molecules. These considerations suggest that the precise interaction between the guaiacol molecule and H_3O^+ plays an important role in modulating the reaction kinetics. To better evaluate the situation, we performed an additional set of ~100-ps-long unbiased AIMD simulations of guaiacol in the five reactive systems and studied their equilibrium behaviour, that is, when no bias is applied.

Table 1 | Summary of the forward and backward rate constants, phenomenological free energy barriers and internal energy barriers (Methods) for the I→IV conversion (Fig. 3a) in the investigated catalytic systems

System	Rate constant (s^{-1})		Phenomenological free energy barrier (kJ mol^{-1})		Internal energy barrier (kJ mol^{-1})
	Forward	Backward	Forward	Backward	
Homogeneous (171 H_2O)	6.36×10^{1}	2.19×10^{1}	112±6	117±6	173
H-BEA (17 H_2O)	1.11×10^{2}	5.86×10^{1}	110.1±0.7	112.8±0.7	132
H-BEA (22 H_2O)	2.40×10^{3}	2.84×10^{2}	97±1	106±1	155
H-BEA (27 H_2O)	1.15×10^{4}	9.12×10^{2}	90±1	101±1	141
H-FAU (22 H_2O)	3.09×10^{1}	1.19×10^{3}	116±1	100±1	124

Note that the backward reaction is affected by the presence of bias walls (Supplementary Methods); the backward rate constant and phenomenological barrier are therefore reported only for completeness.

To analyse the simulations, we introduced in the system, a posteriori, a fictitious proton atom[39,40] (p), as some of us have previously done[30] (Supplementary Methods). This atom follows the location of the hydronium ion, jumping smoothly from oxygen to oxygen based on their surrounding number of protons. Since for **I** → **VI** to occur the hydronium ion must interact with O_m while a water molecule must interact with C_m, we first plotted the probability density of the distance between O_m and the hydronium ion ($d(O_m;p)$) and the minimum distance between the methoxy carbon C_m and all water oxygen atoms O_w ($\min(d(O_w;C_m))$, which is shown in Fig. 7a.

For clarity, we labelled the various quadrants as q1 through q4. Starting from the vertical axis, it is evident that C_m always has at least one water molecule within 4 Å in the homogeneous system (q4), as expected in a solvated environment. A similar pattern is observed in H-FAU (22 H_2O) and H-BEA (27 H_2O). By contrast, a substantial number of states with $\min(d(O_w;C_m)) > 4$ Å (q2) are found for H-BEA with 17 and 22 H_2O, indicating that the unit cell is sufficiently spacious for guaiacol to occasionally move away from the water clusters. More intriguingly, along the horizontal axis, the hydronium ion rarely interacts with O_m, as evidenced by the lack of states sampled in q3 ($d(O_m;p) < 4$ Å). The exceptions are H-BEA with 22 and 27 H_2O, where a distinct concentration of states appears in q3. This observation is notable, as these systems also have the lowest free energy barriers. The facilitated interaction between guaiacol and H_3O^+ is evidently crucial for the system's reactivity, as further supported by the inverse correlation between the average CN between the hydronium ion and O_m ($CN(O_m;p)$) explored during the simulations and the computed reaction barrier (Fig. 7b).

The two high-water-loaded H-BEA zeolites appear to possess a specific feature that enhances the interaction between the hydronium ion and guaiacol molecule. One possibility is that the hydronium ions are under-coordinated in the confined environment of the zeolite[31]. To investigate this, we monitored the CNs between the hydronium ion and surrounding water molecules (Fig. 7c). In the homogeneous system, the hydronium ion is well-solvated, typically surrounded by around

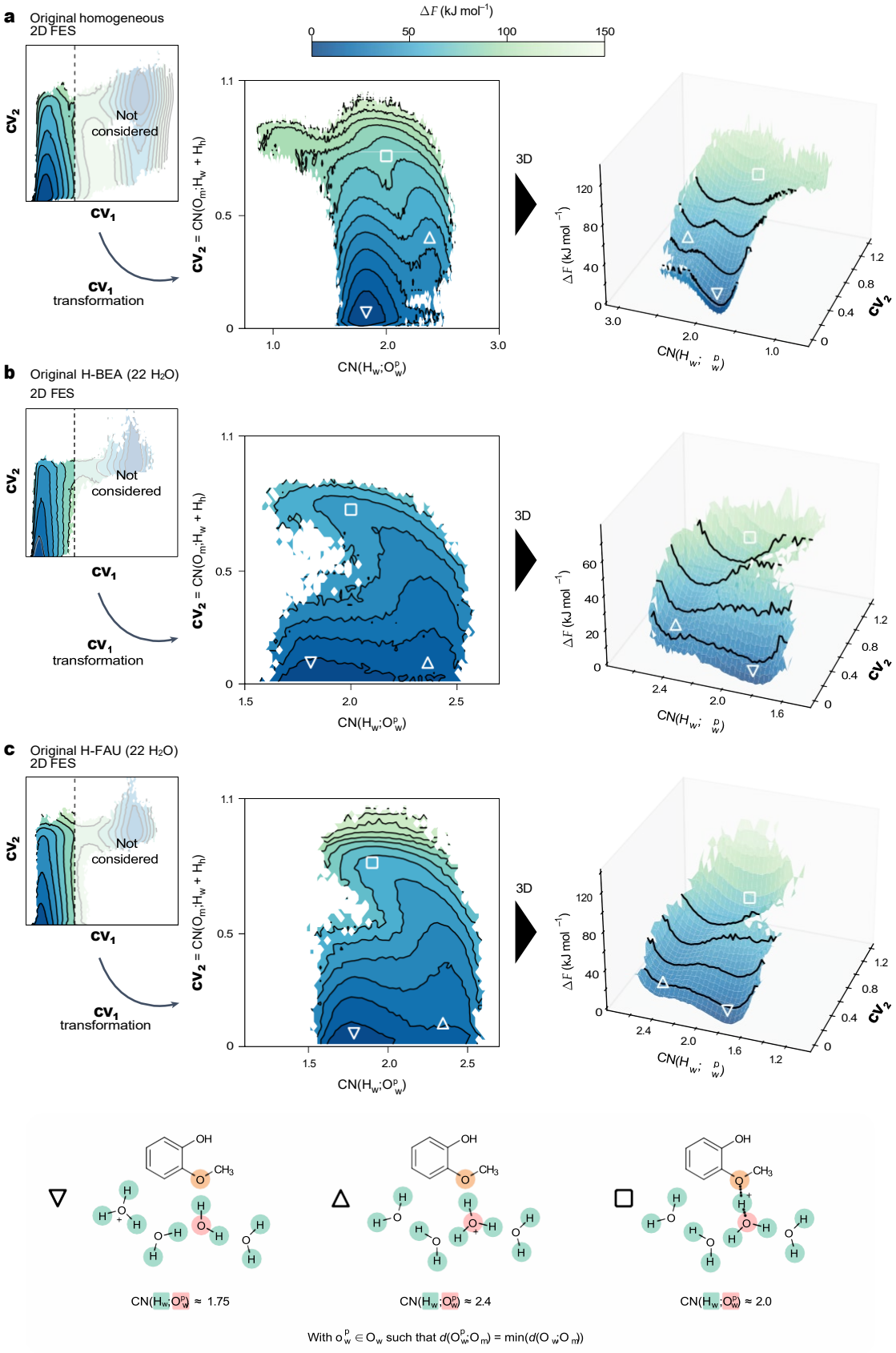

Fig. 6 | Interactions between the hydronium ion and the reactive guaiacol substrate. a–c, The FESs that describe the protonation state of the closest water oxygen (O_w) to the methoxy oxygen (O_m), that is, CN (H_w; O^p_w), as a function of the protonation degree of guaiacol (**CV_2**) for the homogeneous system (**a**), for H-BEA with 22 H_2O (**b**) and for H-FAU with 22 H_2O (**c**). The same FESs are also shown in three-dimensional (3D) plots (right) with black lines placed at **CV_2** = 0.1, 0.3, 0.5 and 0.7, to guide the reader's eye. To obtain such FESs, we transformed **CV_1** in the original FESs (Fig. 4b,c for **a** and **b**, respectively), ignoring states for which **CV_1** > −0.2. Symbols are defined in the bottom panel; 2D, two-dimensional.

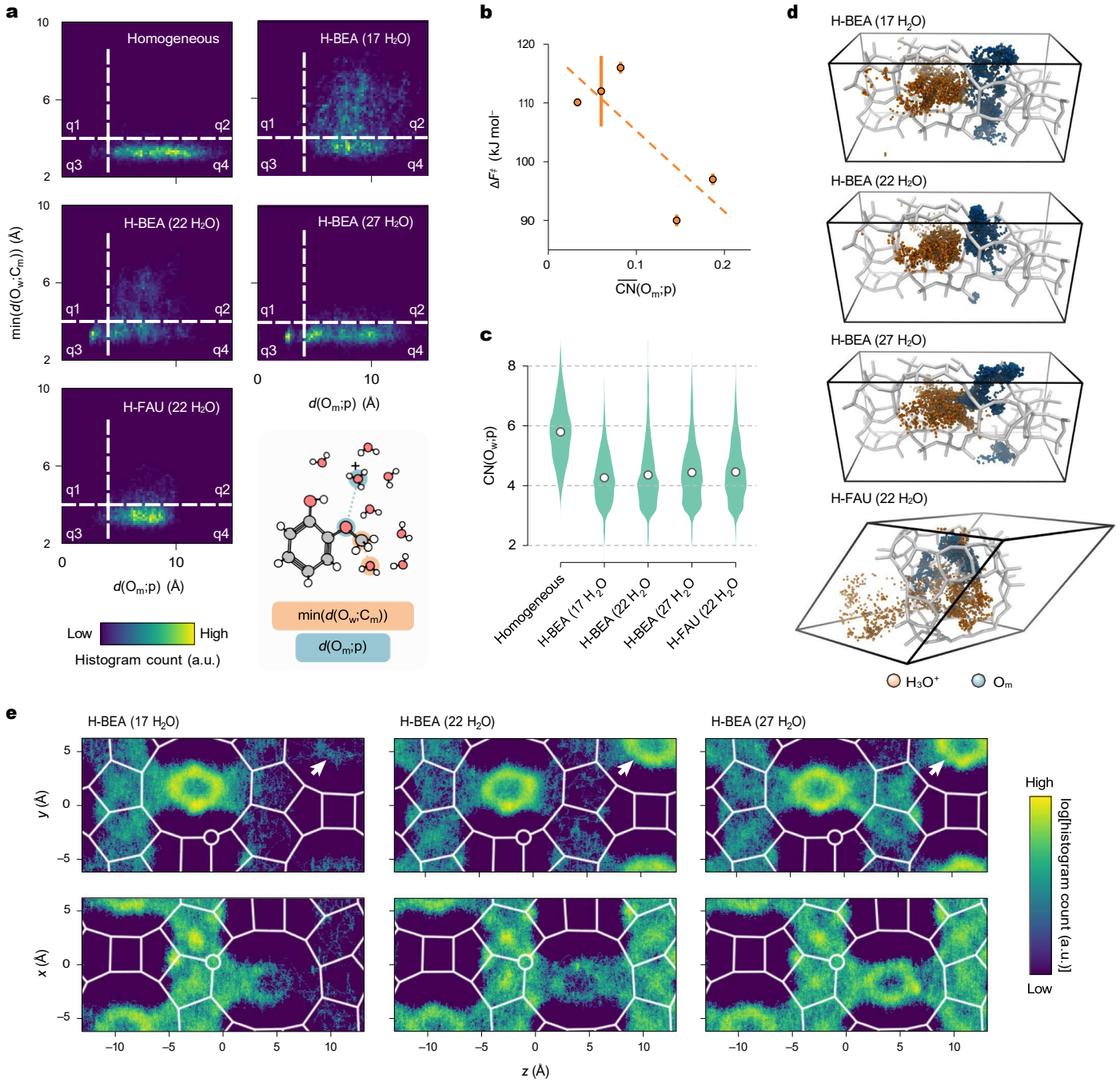

Fig. 7 | The zeolite topology induces a favourable association between the guaiacol and the hydronium ions. a, Distribution of the distance between the methoxy oxygen and the hydronium ion ($d(O_m;p)$) and the minimum distance between water oxygen atoms and the methoxy carbon ($\min(d(O_w;C_m))$), as shown in the schematic at the bottom right. The white dashed lines are placed at 4 Å to guide the reader's eye. **b**, Correlation plot between the phenomenological free energy barrier of the **I** → **VI** reaction (Fig. 3a; $\Delta F^{\ddagger}$) and the average CN between the methoxy oxygen and the hydronium ion ($\overline{CN}(O_m;p)$, d_0 = 4.0 Å; for the definition of d_0, see equation 3 in Supplementary Methods). The error bars on the phenomenological barriers represent a 95% confidence interval computed by interpreting the weighted histogram analysis method as a maximum likelihood estimate, as implemented in ThermoLIB[59] (additional details are reported in Supplementary Methods). **c**, Distribution of the CN between the hydronium ion and the water oxygen atoms ($CN(O_w;p)$, d_0 = 3.6 Å, n = 16, m = 28; for the definitions of d_0, n and m, see equation 3 in Supplementary Methods). The white dot highlights the distribution mean. **d**, Three-dimensional visualization of the positions explored by the hydronium ion (in orange) and the methoxy oxygen (O_m; in blue) during the AIMD simulations every 50 fs. **e**, Density plots for the water oxygen atoms in the H-BEA unit cell collected during the AIMD simulations, as a function of the water loading. The white lines provide an indication of the Si atom network, while the small white circle highlights the location of the Al defect. Note that the heat map colours are in a logarithmic scale.

six water molecules. By contrast, within the confined zeolite channels, the solvation drops to about four water molecules for all zeolite catalytic systems. This reduced solvation could lower the internal reaction energy, a hypothesis we confirmed by calculating internal energy barriers for all systems (Table 1 and Supplementary Fig. 27). Despite some uncertainty due to challenges in converging the ensemble averages, all zeolite models exhibit internal energy barriers lower than those in the homogeneous case. These results suggest that under-coordination in confined environments increases the electrophilicity—and thus the reactivity—of the hydronium ions. In other words, the hydronium ions

are more likely to protonate the reactive substrate, which reduces the enthalpic requirement ofthe reaction. This finding isconsistent with the lower activation energy observed in the experimental Arrhenius plot for the heterogeneous system compared to the homogeneous one (Fig. 1).

The final question to address is why H-FAU (22 H_2O) and H-BEA (17 H_2O) exhibit such high phenomenological free energy barriers. To explore this, we investigated the mobility of key species involved in the reaction across the different zeolite systems. We tracked the relative positions of O_m and H_3O^+ throughout the simulations, shown in Fig. 7d as orange (H_3O^+) and blue (O_m) points. The cloud of orange points, representing the hydronium ion's oxygen locations, reveals that in all H-BEA models, the hydronium ion remains confined within the channel where the aluminium defect is located, indicating limited mobility. By contrast, in H-FAU, the hydronium ion exhibits much higher mobility, freely exploring the large cages within the unit cell. This increased mobility appears to be an entropically driven effect due to the H-FAU pore architecture, rather than being caused by electrostatic interactions, as the average distance between the proton and the Al defect is greater in H-FAU compared to the H-BEA models (Supplementary Fig. 29). We suggest that this higher mobility leads to a greater entropic loss when bringing the hydronium ion into contact with guaiacol, thereby increasing the overall free energy barrier.

This hypothesis is unable to explain the high barrier for H-BEA (17 H_2O). There, one can see how O_m is somehow more mobile in the zeolite channel (Fig. 7d) compared to the higher loadings. If one looks at the water density in the pores (Fig. 7e), one can see how the channel that does not contain the Al defect (indicated by a small white arrow in Fig. 7e) is mostly empty with 17 H_2O, while it becomes quite filled with water at the higher loadings. During the simulations of H-BEA (17 H_2O), the guaiacol tends to move towards these empty hydrophobic channels away from the water, limiting the interactions with the water cluster containing the hydronium ion. This separation effect is likely also responsible for the higher barrier of **I** → **II** in H-BEA (22 H_2O) than in the homogeneous case (Fig. 3c). Indeed, when evaluating the distribution of distances between the hydronium ion and the aromatic *para* carbon, we noticed that, in the zeolite, guaiacol preferentially exposes the two hydrophilic oxygenated groups to the water cluster, keeping the aromatic carbon away from it (Supplementary Fig. 28). This creates a lack of interactions under 4 Å; these interactions are still present in the homogeneous case, being that the molecule is fully surrounded by water. Overall, these local organizational considerations highlight how entropy plays a key role in the activity of zeolites in water. The design of new active catalysts should not focus only on the shape of the catalytic pocket, but also on the solvent loading and molecular organization in the pores, which could be tweaked (for instance) by the ad hoc introduction of hydrophilic sites such as silanol nests[41].

Conclusions

Brønsted-acid-catalysed reactions in HPW are notoriously complex, posing remarkable challenges for both experimental and theoretical studies. In this work we explored the mechanistic aspects of the *O*-demethylation of guaiacol in water (hydrolysis)—a realistic model compound for lignin-derived platform chemicals—into catechol using a combined computational and experimental approach. Through a comprehensive set of enhanced-sampling AIMD simulations, we accurately accounted for the water solvent and the effect of local confined environments under operational conditions. Our focus was on the differences in the reactivity and behaviour of water and hydronium ions in bulk versus their confinement within the micropores of zeolites for the acid-catalysed bimolecular hydrolysis reaction.

Our simulations suggest that the reaction predominantly follows a COA-S_N2 mechanism, without forming a stable or metastable oxonium ion but instead involving an ionic contact pair between the reacting guaiacol and hydronium ion. This mechanism is supported by experiments with various *O*-alkylcatechols and a pronounced inverse SKIE. Theoretical predictions align with these findings, indicating that proton transfer is completed at the COA-S_N2 transition state, with non-reactive hydrogens contributing to the inverse SKIE.

Moreover, the simulations highlight the crucial role of confinement within zeolite micropores in modulating reaction kinetics and enhancing the reactivity of hydronium ions, accelerating the COA-S_N2 hydrolysis reaction. Partial under-coordination of the hydronium ion within these confined spaces increases its electrophilicity, leading to a lower internal energy barrier for the reaction. This effect is consistent across all the zeolite models studied and aligns well with experimental kinetic data, where the Arrhenius activation energy for catalytic turnover is significantly lower in the zeolite catalyst compared to the homogeneous system. In H-BEA, the free energy barrier is notably sensitive to the water loading, as excess solvent can enhance the interaction between guaiacol and the hydronium ion. Therefore, an effective catalyst must not only favour the right molecular organization of solvent and reactant, but also an optimal number of water molecules to maximize substrate–hydronium ion contact. This is not the case in H-FAU, where the hydronium ion's greater mobility interferes with its interaction with guaiacol.

In conclusion, we provide strong evidence that the local molecular organization of solvents and reactants around a confined catalytic active site are crucial factors driving the enhanced turnover activity of hydronium ions. The findings and the associated molecular insights go well beyond those of previous studies, which primarily focused on monomolecular elimination reactions of water from simple alcohols with charged intermediates, by extending to bimolecular substitution reactions involving water as a reactant. Overall, this work contributes to a deeper understanding of the complex chemistry of water in confined environments, which is vital for advancing the circular bioeconomy.

Methods

Atomistic models of the two catalytic systems

Both the homogeneous and heterogeneous catalytic systems were modelled by means of periodic simulations. The unit cells are graphically depicted in Fig. 3b. The homogeneous system accounts for two solvation layers around the guaiacol molecule (171 water molecules). The loading of water in the heterogeneous system was roughly estimated with classical grand canonical Monte Carlo simulations to be 22 water molecules. Both systems account for a single active site, being an additional proton in the homogeneous system or a single aluminium substitution in the heterogeneous unit cell. While it is known that zeolites can easily undergo fast and reversible bond breaking and formation when exposed to liquid water, we here focus on a pristine Brønsted acid site to obtain general reactivity trends while leaving the more complex effects related to the formation of framework-associated and extra-framework aluminium species for future investigations. The unit cells of both the homogeneous and heterogeneous systems were equilibrated in the isothermal–isobaric ensembles, and the average unit cell parameters (18.7 Å × 18.7 Å × 18.7 Å for the homogeneous system and 12.7 Å × 12.7 Å × 26.7 Å for the heterogeneous one, with all angles of 90°) were subsequently used in the AIMD production runs in the NVT ensemble. A more extensive explanation of the system preparation is in Supplementary Methods.

Enhanced-sampling AIMD simulations

Production runs to investigate the reactive systems were performed by means of AIMD simulations based on density functional theory, aiming for an accurate description of entropic effects at the complex operating conditions at which the reaction takes place. We employed the CP2K software[42,43] (v.5.1) in combination with the BLYP-D3 functional[44–46] and a TZVP-quality basis set. The energy cut-off for the complementary plane-wave basis set[47] was fixed at 300 Ry, and Goedecker–Teter–Hutter pseudopotentials[48] were used to smooth the electron density in proximity of the nuclei. The convergence criterion for the

self-consistent field was set at 10^{-5} Hartree units. The equations of motion were integrated with a time step of 0.5 fs using a chain of five Nosé–Hoover thermostats[49,50] for temperature control (523 K). To sample activated events, which would not spontaneously occur in regular AIMD given the accessible timescales, enhanced-sampling simulations were performed by coupling the PLUMED library[51] to CP2K. The CVs used to drive the reaction were chosen to be a CN or a linear combination of CNs. Additional details concerning the simulations are reported in Supplementary Methods. Figure 4a reports a schematic depiction of the CV used to bias the COA-S_N2 reaction, as we found it to be the dominant mechanism of the demethylation process.

To obtain the final FESs, we used a two-step approach where a multiple-walkers[52] well-tempered[53] metadynamics[54] simulation was first performed to screen the selected CV and obtain an initial FES estimate. We used 4–10 parallel walkers, a bias factor of 10–12, an initial hills height of 2–4 kJ mol^{-1}, a hills width of 0.03 and a deposition pace of 50 fs. The exact values changed depending on the specific reaction, with the choice being driven by practical tests, but they are of negligible importance for the final result. The FES estimate from metadynamics, obtained by summing the spawned hills, was then reverted and applied as bias in a subsequent US simulation[55,56] along the same CV. In US, a set of quadratic bias potentials (the umbrellas) is distributed along the CV range of interest. By referring to the CV as q, each of the umbrellas is centred at a specific CV value $q = q_0$ and has a force constant κ (typically around 250 kJ mol^{-1}, in our case), giving the bias form as follows:

$$U_b(q) = \frac{K}{2}(q - q_0)^2. \quad (2)$$

As rule of thumb, we separated the umbrella centres with a $\Delta q_0 \approx 0.1$. Additional umbrellas with a different spacing or a tighter κ were sometimes added to improve sampling in difficult regions along the chosen CV or CVs. The final FES estimates were obtained with the weighted histogram analysis method[57,58], accounting for the overall bias (umbrella plus inverse of the metadynamics FES estimate) as implemented in our in-house-developed Python package, ThermoLIB[59].

For some reactions, a two-dimensional CV space is needed to satisfactorily explore the possible reactive paths. In that case, we either directly performed two-dimensional US simulations (extracting the final FES with a two-dimensional weighted histogram analysis method) or we transformed the original FES along a new set of CVs using the statistical analysis tools of ThermoLIB, as already done in previous publications[30,60]. Finally, ThermoLIB was also used to compute the kinetic constant of the reactions under study in the transition state theory approximation[60,61] (Supplementary Methods).

Experimental methods

The guaiacol demethylation reaction was investigated experimentally in high-pressure equipment using both the homogeneous and heterogeneous catalysts. The experimental procedures are reported extensively in Supplementary Methods, while an extensive explanation of the experimental results can be found in Supplementary Notes 2 and 3 for the homogeneous and heterogeneous catalyses, respectively. There, we also highlight additional (both successful and unsuccessful) experiments that were performed to unravel the reaction mechanism. The synthesis of the guaiacol derivatives used to assess the validity of the COA-S_N2 mechanism is reported in the Supplementary Methods; the respective NMR spectra used to characterize the synthesized compounds are reported in Supplementary Note 4.

Data availability

Example of CP2K input file, the initial and final structures of the AIMD simulations and the relative PLUMED input files are provided as Supplementary Data. Any additional data are available from the authors upon request. Extended computational details and results discussion are presented in Supplementary Information.

Code availability

ThermoLIB, the software used to compute the free energy surfaces and reaction rates from the enhanced-sampling simulations, is available upon request at https://molmod.ugent.be/software/thermolib.

References

1. Sheldon, R. A. Biocatalysis and biomass conversion: enabling a circular economy. *Philos. Trans. R. Soc. A* **378**, 20190274 (2020).
2. Mazmanian, D. A., Jurewitz, J. & Nelson, H. T. A governing framework for climate change adaptation in the built environment. *Ecol. Soc.* **18**, 56 (2013).
3. Liao, Y. H. et al. A sustainable wood biorefinery for low-carbon footprint chemicals production. *Science* **367**, 1385–1390 (2020).
4. Graglia, M., Kanna, N. & Esposito, D. Lignin refinery: towards the preparation of renewable aromatic building blocks. *ChemBioEng Rev.* **2**, 377–392 (2015).
5. Schutyser, W. et al. Chemicals from lignin: an interplay of lignocellulose fractionation, depolymerisation, and upgrading. *Chem. Soc. Rev.* **47**, 852–908 (2018).
6. Bartling, A. W. et al. Techno-economic analysis and life cycle assessment of a biorefinery utilizing reductive catalytic fractionation. *Energy Environ. Sci.* **14**, 4147–4168 (2021).
7. Ha, J. M. et al. Recent progress in the thermal and catalytic conversion of lignin. *Renew. Sust. Energ. Rev.* **111**, 422–441 (2019).
8. Zakzeski, J., Bruijnincx, P. C. A., Jongerius, A. L. & Weckhuysen, B. M. The catalytic valorization of lignin for the production of renewable chemicals. *Chem. Rev.* **110**, 3552–3599 (2010).
9. Vanholme, R., Demedts, B., Morreel, K., Ralph, J. & Boerjan, W. Lignin biosynthesis and structure. *Plant Physiol.* **153**, 895–905 (2010).
10. Liu, X. D. et al. Recent advances in the catalytic depolymerization of lignin towards phenolic chemicals: a review. *ChemSusChem* **13**, 4296–4317 (2020).
11. Sheldon, R. A. Green and sustainable manufacture of chemicals from biomass: state of the art. *Green Chem.* **16**, 950–963 (2014).
12. Fiege, H. et al. Phenol Derivatives. in *Ullmann's Encyclopedia of Industrial Chemistry* (John Wiley & Sons, Ltd, 2000).
13. Sun, Z. H., Fridrich, B., de Santi, A., Elangovan, S. & Barta, K. Bright side of lignin depolymerization: toward new platform chemicals. *Chem. Rev.* **118**, 614–678 (2018).
14. Zhang, L. L. & Hu, G. P. Supply chain design and operational planning models for biomass to drop-in fuel production. *Biomass Bioenergy* **58**, 238–250 (2013).
15. Cheng, F. & Brewer, C. E. Producing jet fuel from biomass lignin: potential pathways to alkyl benzenes and cycloalkanes. *Renew. Sustain. Energy Rev.* **72**, 673–722 (2017).
16. Zhao, S. & Abu-Omar, M. M. Renewable thermoplastics based on lignin-derived polyphenols. *Macromolecules* **50**, 3573–3581 (2017).
17. Siragusa, F. et al. Access to biorenewable and CO_2-based polycarbonates from exovinylene cyclic carbonates. *ACS Sustain. Chem. Eng.* **9**, 1714–1728 (2021).
18. Wu, X. et al. Advancements and perspectives toward lignin valorization via O-demethylation. *Angew. Chem. Int. Ed.* **63**, e202317257 (2023).
19. Yang, L., Seshan, K. & Li, Y. D. A review on thermal chemical reactions of lignin model compounds. *Catal. Today* **298**, 276–297 (2017).
20. Bomon, J. et al. Efficient demethylation of aromatic methyl ethers with HCl in water. *Green Chem.* **23**, 1995–2009 (2021).
21. Alder, C. M. et al. Updating and further expanding GSK's solvent sustainability guide. *Green Chem.* **18**, 3879–3890 (2016).
22. Wu, X. Y., Fu, J. & Lu, X. Y. Kinetics and mechanism of hydrothermal decomposition of lignin model compounds. *Ind. Eng. Chem. Res.* **52**, 5016–5022 (2013).

23. Yang, L., Zhou, W., Seshan, K. & Li, Y. D. Green and efficient synthesis route of catechol from guaiacol. *J. Mol. Catal. A Chem.* **368**, 61–65 (2013).
24. Li, Z., Sutandar, E., Goihl, T., Zhang, X. & Pan, X. J. Cleavage of ethers and demethylation of lignin in acidic concentrated lithium bromide (ACLB) solution. *Green Chem.* **22**, 7989–8001 (2020).
25. Bomon, J. et al. Bronsted acid catalyzed tandem defunctionalization of biorenewable ferulic acid and derivates into bio-catechol. *Angew. Chem. Int. Ed.* **59**, 3063–3068 (2020).
26. Ennaert, T. et al. Potential and challenges of zeolite chemistry in the catalytic conversion of biomass. *Chem. Soc. Rev.* **45**, 584–611 (2016).
27. Wu, X. et al. Lignin-first monomers to catechol: rational cleavage of C–O and C–C bonds over zeolites. *ChemSusChem* **15**, e202102248 (2022).
28. Stanciakova, K. & Weckhuysen, B. M. Water-active site interactions in zeolites and their relevance in catalysis. *Trends Chem.* **3**, 456–468 (2021).
29. Bates, J. S., Bukowski, B. C., Greeley, J. & Gounder, R. Structure and solvation of confined water and water–ethanol clusters within microporous Brönsted acids and their effects on ethanol dehydration catalysis. *Chem. Sci.* **11**, 7102–7122 (2020).
30. Bocus, M., Vanduyfhuys, L., De Proft, F., Weckhuysen, B. M. & Van Speybroeck, V. Mechanistic characterization of zeolite-catalyzed aromatic electrophilic substitution at realistic operating conditions. *JACS Au* **2**, 502–514 (2022).
31. Bregante, D. T. et al. The shape of water in zeolites and its impact on epoxidation catalysis. *Nat. Catal.* **4**, 797–808 (2021).
32. Liu, Q. & van Bokhoven, J. A. Water structures on acidic zeolites and their roles in catalysis. *Chem. Soc. Rev.* **53**, 3065–3095 (2024).
33. Liu, Y. S. et al. Enhancing the catalytic activity of hydronium ions through constrained environments. *Nat. Commun.* **8**, 14113 (2017).
34. Eckstein, S. et al. Influence of hydronium ions in zeolites on sorption. *Angew. Chem. Int. Ed.* **58**, 3450–3455 (2019).
35. Pfriem, N. et al. Role of the ionic environment in enhancing the activity of reacting molecules in zeolite pores. *Science* **372**, 952–957 (2021).
36. Shi, H. et al. Tailoring nanoscopic confines to maximize catalytic activity of hydronium ions. *Nat. Commun.* **8**, 15442 (2017).
37. Bigeleisen, J. Correlation of kinetic isotope effects with chemical bonding in three-centre reactions. *Pure Appl. Chem.* **8**, 217–224 (1964).
38. Kresge, A. J. & Onwood, D. P. Secondary isotope effect on proton transfer from hydronium ion in aqueous solution. *J. Am. Chem. Soc.* **86**, 5014–5016 (1964).
39. Pérez de Alba Ortíz, A., Tiwari, A., Puthenkalathil, R. C. & Ensing, B. Advances in enhanced sampling along adaptive paths of collective variables. *J. Chem. Phys.* **149**, 072320 (2018).
40. Grifoni, E., Piccini, G. & Parrinello, M. Microscopic description of acid–base equilibrium. *Proc. Natl Acad. Sci. USA* **116**, 4054–4057 (2019).
41. Bukowski, B. C., Bates, J. S., Gounder, R. & Greeley, J. Defect-mediated ordering of condensed water structures in microporous zeolites. *Angew. Chem. Int. Ed.* **58**, 16422–16426 (2019).
42. VandeVondele, J. et al. QUICKSTEP: fast and accurate density functional calculations using a mixed Gaussian and plane waves approach. *Comput. Phys. Commun.* **167**, 103–128 (2005).
43. Kuhne, T. D. et al. CP2K: an electronic structure and molecular dynamics software package - Quickstep: efficient and accurate electronic structure calculations. *J. Chem. Phys.* **152**, 194103 (2020).
44. Becke, A. D. Density-functional exchange-energy approximation with correct asymptotic behavior. *Phys. Rev. A* **38**, 3098–3100 (1988).
45. Lee, C. T., Yang, W. T. & Parr, R. G. Development of the Colle-Salvetti correlation-energy formula into a functional of the electron density. *Phys. Rev. B* **37**, 785–789 (1988).
46. Grimme, S., Antony, J., Ehrlich, S. & Krieg, H. A consistent and accurate *ab initio* parametrization of density functional dispersion correction (DFT-D) for the 94 elements H-Pu. *J. Chem. Phys.* **132**, 154104 (2010).
47. Lippert, G., Hutter, J. & Parrinello, M. The Gaussian and augmented-plane-wave density functional method for ab initio molecular dynamics simulations. *Theor. Chem. Acc.* **103**, 124–140 (1999).
48. Goedecker, S., Teter, M. & Hutter, J. Separable dual-space Gaussian pseudopotentials. *Phys. Rev. B* **54**, 1703–1710 (1996).
49. Martyna, G. J., Klein, M. L. & Tuckerman, M. Nosé–Hoover chains: the canonical ensemble via continuous dynamics. *J. Chem. Phys.* **97**, 2635–2643 (1992).
50. Nosé, S. A molecular dynamics method for simulations in the canonical ensemble. *Mol. Phys.* **52**, 255–268 (1984).
51. Tribello, G. A., Bonomi, M., Branduardi, D., Camilloni, C. & Bussi, G. PLUMED 2: new feathers for an old bird. *Comput. Phys. Commun.* **185**, 604–613 (2014).
52. Raiteri, P., Laio, A., Gervasio, F. L., Micheletti, C. & Parrinello, M. Efficient reconstruction of complex free energy landscapes by multiple walkers metadynamics. *J. Phys. Chem. B* **110**, 3533–3539 (2006).
53. Barducci, A., Bussi, G. & Parrinello, M. Well-tempered metadynamics: a smoothly converging and tunable free-energy method. *Phys. Rev. Lett.* **100**, 020603 (2008).
54. Laio, A. & Parrinello, M. Escaping free-energy minima. *Proc. Natl Acad. Sci. USA* **99**, 12562–12566 (2002).
55. Torrie, G. M. & Valleau, J. P. Monte Carlo free energy estimates using non-Boltzmann sampling: application to the sub-critical Lennard-Jones fluid. *Chem. Phys. Lett.* **28**, 578–581 (1974).
56. Torrie, G. M. & Valleau, J. P. Monte Carlo study of a phase-separating liquid mixture by umbrella sampling. *J. Chem. Phys.* **66**, 1402–1408 (1977).
57. Kumar, S., Bouzida, D., Swendsen, R. H., Kollman, P. A. & Rosenberg, J. M. The weighted histogram analysis method for free-energy calculations on biomolecules. I. The method. *J. Comput. Chem.* **13**, 1011–1021 (1992).
58. Souaille, M. & Roux, B. Extension to the weighted histogram analysis method: combining umbrella sampling with free energy calculations. *Comput. Phys. Commun.* **135**, 40–57 (2001).
59. Vanduyfhuys, L. ThermoLIB (Center for Molecular Modeling); https://molmod.ugent.be/software/thermolib
60. Bailleul, S. et al. Ab initio enhanced sampling kinetic study on MTO ethene methylation reaction. *J. Catal.* **388**, 38–51 (2020).
61. Van Speybroeck, V., Bocus, M., Cnudde, P. & Vanduyfhuys, L. Operando modeling of zeolite-catalyzed reactions using first-principles molecular dynamics simulations. *ACS Catal.* **13**, 11455–11493 (2023).

Acknowledgements

We acknowledge financial support from the Research Foundation Flanders (FWO; BioFact Excellence of Science project grant no. 30902231). The computational resources and services used were provided by Ghent University (Stevin Supercomputer Infrastructure) and the VSC (Flemish Supercomputer Center), funded by Ghent University, FWO and the Flemish Government. E.V.D.B, M. Bocus, L.V. and V.V.S. acknowledge funding from FWO. V.V.S. and L.V. acknowledge the Research Board of Ghent University. B.U.W.M. thanks the Francqui Foundation for an appointment as Collen-Francqui professor and UAntwerp for BOF GOA support (36083). X.W. thanks the Chinese Scholarship Council (no. 201806890016) for financial support. Finally, we thank R. Goeminne for his assistance with the grand canonical Monte Carlo simulations.

Author contributions

M. Bocus, E.V.D.B., V.V.S., B.U.W.M. and B.F.S. initiated the discussion and designed the scope of the project. E.V.D.B. and M. Bocus conceived and coordinated the research under the supervision of V.V.S.; E.V.D.B. and M. Bocus performed all calculations based on density functional theory and related to the homogeneously catalysed and heterogeneously catalysed systems, respectively, under the supervision of V.V.S.; M. Bal performed all the kinetic experiments for the homogeneously catalysed *O*-dealkylation under the supervision of B.U.W.M.; X.W. performed all the kinetic experiments for the heterogeneously catalysed *O*-dealkylation under the supervision of B.F.S.; J.B. performed the initial O dealkylation reactions to unravel its S_N character and the labelled water experiments under the supervision of B.U.W.M.; and L.V. was responsible for the development of the ThermoLIB library used for the analysis of all enhanced-sampling simulations and provided guidance throughout. M. Bocus, E.V.D.B. and V.V.S. wrote the first version of the paper, which was revised with input from all other co-authors. M. Bocus and V.V.S. drafted the final version of the paper and Supplementary Information.

Competing interests

The authors declare no competing interests.

Additional information

Supplementary information The online version contains supplementary material available

Correspondence and requests for materials should be addressed to Bert F. Sels, Bert U. W. Maes or Veronique Van Speybroeck.